Journal of
Materials Chemistry C

Materials for optical, magnetic and electronic devices

rsc.li/materials-c

ROYAL SOCIETY
OF **CHEMISTRY**
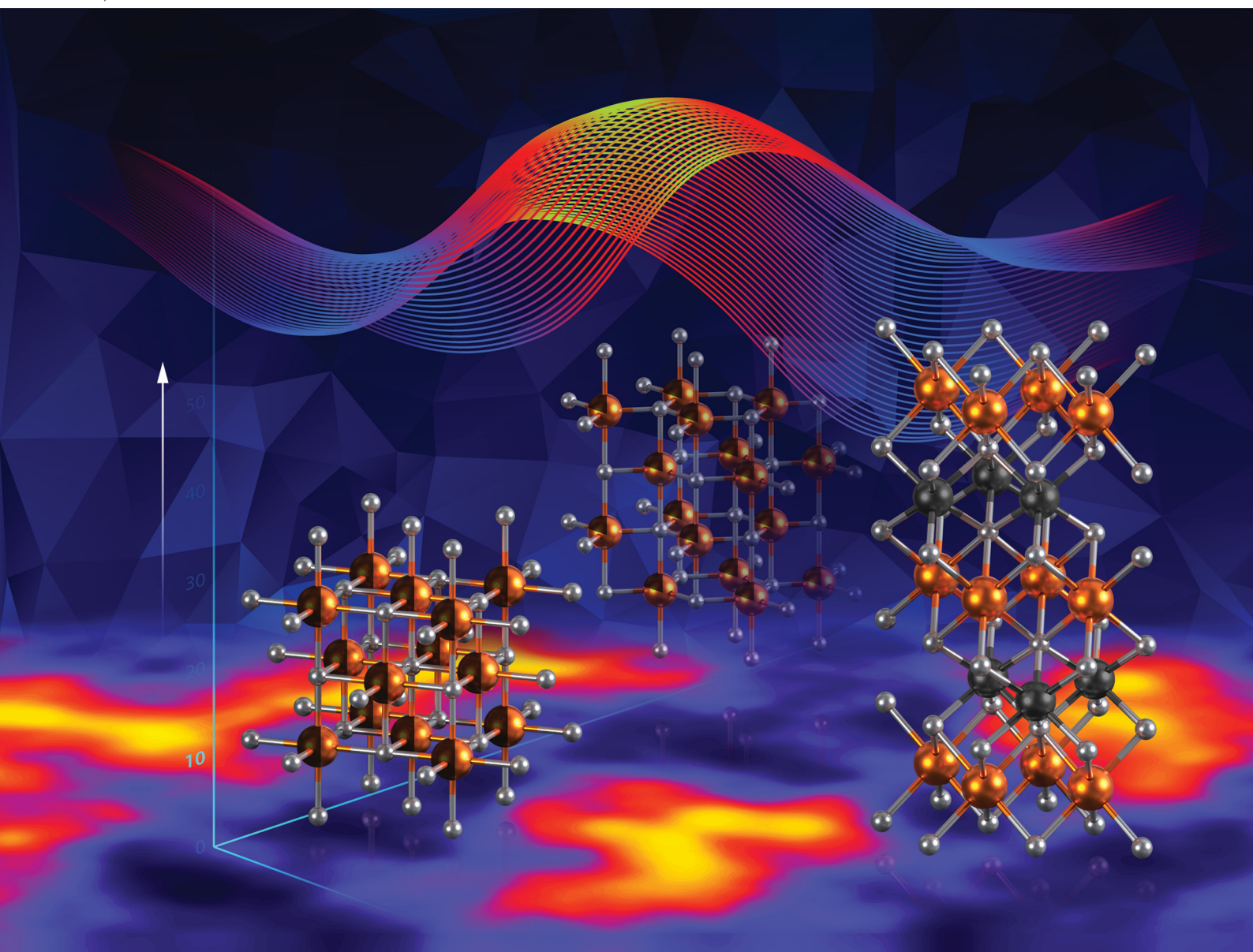
PAPER
Andriy Zakutayev *et al.*
Bulk and film synthesis pathways to ternary magnesium
tungsten nitrides

10 YEARS
ANNIVERSARY

Journal of Materials Chemistry C

PAPER

Check for updates

Bulk and film synthesis pathways to ternary magnesium tungsten nitrides†

Christopher L. Rom, [ID] [ab] Rebecca W. Smaha, [ID] [a] Callan A. Knebel, [ID] [b]
Karen N. Heinselman, [ID] [a] James R. Neilson, [ID] [bc] Sage R. Bauers [ID] [a] and
Andriy Zakutayev [ID] *[a]

Bulk solid state synthesis of nitride materials usually leads to thermodynamically stable, cation-ordered crystal structures, whereas thin film synthesis tends to favor disordered, metastable phases. This dichotomy is inconvenient both for basic materials discovery, where non-equilibrium thin film synthesis methods can be useful to overcome reaction kinetic barriers, and for practical technology applications where stable ground state structures are sometimes required. Here, we explore the uncharted Mg–W–N chemical phase space using rapid thermal annealing to reconcile the differences between thin film (on ambient or heated substrates) and bulk powder syntheses. Combinatorial co-sputtering synthesis from Mg and W targets in a N_2 environment yielded cation-disordered Mg–W–N phases in the rocksalt (0.1 < Mg/(Mg + W) < 0.9), and hexagonal boron nitride (0.7 < Mg/(Mg + W) < 0.9) structure types. In contrast, bulk synthesis produced a cation-ordered polymorph of $MgWN_2$ that consists of alternating layers of rocksalt-like $[MgN_6]$ octahedra and nickeline-like $[WN_6]$ trigonal prisms (denoted "rocksaline"). Thermodynamic calculations corroborate these observations, showing rocksaline $MgWN_2$ is stable while other polymorphs are metastable. We also show that rapid thermal annealing can convert disordered rocksalt films to this cation-ordered polymorph, but only near the $MgWN_2$ stoichiometry. Electronic structure calculations suggest that this rocksalt-to-rocksaline structural transformation should also drive a metallic-to-semiconductor transformation. In addition to revealing three new phases (rocksalt $MgWN_2$ and Mg_3WN_4, hexagonal boron nitride Mg_3WN_4, and rocksaline $MgWN_2$), these findings highlight how rapid thermal annealing can control polymorphic transformations, adding a new strategy for exploration of thermodynamic stability in uncharted phase spaces.

1 Introduction

Ternary nitrides are an emerging class of ceramic materials with applications in solid-state lighting, electrochemical energy storage, optoelectronics, piezoelectrics, ferroelectrics, and wide-bandgap semiconductor devices.[1] However, nitrides are under-explored, lagging behind oxides with an order of magnitude fewer scientific publications and known structures.[1–3] Therefore, exploring chemical phase space to find new ternary nitrides will open avenues to identifying novel materials with intriguing

functional properties that may underlie future technologies. Recent breakthroughs in high-throughput computational techniques successfully predicted many new ternary nitrides,[3] and combinatorial co-sputtering has proven to be a powerful tool for experimentally realizing these predicted materials.[3–15]

In particular, Mg and Zn can be combined with early transition metals and main-group elements to form ternary nitrides that are structurally related to the binary $M^{3+}N$ nitrides (*e.g.*, wurtzite GaN or rocksalt TiN).[4] With A as Zn or Mg and M as a main group or transition metal, the stoichiometries $A^{2+}M^{4+}N_2$, $A_2^{2+}M^{5+}N_3$, and $A_3^{2+}M^{6+}N_4$ have the 1 : 1 cation : anion ratio of $M^{3+}N$ compounds, and semiconducting properties emerge when M is a d^0 transition metal or a main-group element.[4,16] Furthermore, Zn and Mg favor 4- or 6-fold coordination, respectively, and therefore tend to produce the respective wurtzite-derived or rocksalt-derived structures. For example, exploration of the Zn–Mo–N phase space by combinatorial sputtering revealed a wurtzite-like structure across a range of compositions, from metallic $ZnMoN_2$ to semiconducting wurtzite-like Zn_3MoN_4 (with a bandgap of 2.4 eV).[17] Similarly, the Mg–W–N

[a] Materials Science Center, National Renewable Energy Laboratory, Golden, CO 80401, USA. E-mail: Andriy.Zakutayev@nrel.gov

[b] Department of Chemistry, Colorado State University, Fort Collins, CO, 80523, USA

[c] School of Advanced Materials Discovery, Colorado State University, Fort Collins, CO, 80523, USA

† Electronic supplementary information (ESI) available: Additional experimental details, Mg-poor phases, crystallographic details, annealing experiments, simulating cation disorder, RBS measurements, AES measurements, electronic structure calculations, electronic property measurements. See DOI: https://doi.org/10.1039/d3tc02059b

phase space is a promising area of exploration because W has multiple possible oxidation states (between 0 and 6+, inclusive), potentially leading to varied structures and properties.

Combinatorial co-sputtering is a good choice to rapidly survey this potentially complex phase space. However, materials discovered by combinatorial sputtering often deviate from those predicted by computational methods or synthesized in bulk on a key detail: cation (dis)order.[4,18] This discrepancy can potentially be beneficial, such as when cation-disorder lowers the bandgap into the visible range.[8,18] In other cases, cation disorder negatively impacts optoelectronic properties by localizing charge carriers[18,19] or even leading to polymorphism.[10] How to control this structural polymorphism and cation disorder is still an open question. For example, annealing conditions are known to affect the degree of cation (dis)order,[20,21] but that control is often material-specific and difficult to explore in a high-throughput manner.[18] Therefore, understanding metastable phase formation and cation (dis)order in ternary nitrides remains a pressing challenge for the field to fully realize the tunable properties of this promising class of materials.

In this article, we describe the discovery of several new Mg–W–N compounds in this previously-unexplored ternary phase space. We show that thin film combinatorial co-sputtering methods yielded cation-disordered rocksalt (RS, space group $Fm\bar{3}m$, $0.1 < $ Mg/(Mg + W) $ < 0.9$) and hexagonal boron nitride structures (h-BN, space group $P6_3/mmc$, $0.7 < $ Mg/(Mg + W) $ < 0.9$) covering the $MgWN_2$ and Mg_3WN_4 stoichiometries. In contrast, our bulk ceramic methods yielded cation-ordered $MgWN_2$ with space group $P6_3/mmc$. We call this cation-ordered structure "rocksaline" (RL) as a portmanteau of the rocksalt-like Mg^{2+} and nickeline-like W^{4+} layers. Thermodynamic calculations confirm that the RL polymorph is the ground state of the $MgWN_2$ composition. Rapid thermal annealing (RTA) of thin films converted the disordered RS structure to this ordered RL structure in a narrow composition window near the $MgWN_2$ stoichiometry, resolving this difference between the thin film and the bulk synthesis results. The Mg_3WN_4 was only produced in thin films, and formed in either the RS or h-BN structure. Thermodynamic calculations reveal these polymorphs to be close in energy to one another and slightly metastable. Electronic structure calculations suggest that RL $MgWN_2$ should be a semiconductor, while RS $MgWN_2$ should be metallic. Resistivity measurements of the synthesized films as a function of composition and temperature show both RL $MgWN_2$ and RS Mg_3WN_4 are semiconducting, but we were unable to verify the charge transport behavior of RS $MgWN_2$. These findings show how RTA treatment of disordered films can build upon existing combinatorial co-sputtering techniques to rapidly assess the thermodynamic synthesizability of a predicted cation-ordered phase.

2 Methods

2.1 Bulk synthesis and characterization

Powders of Mg_3N_2 (Alfa Aesar, $>99.6\%$, 325 mesh) and W (Sigma-Aldrich, 99%, 42 μm) were used as received. As these reagents are air sensitive, they were prepared and stored in an argon-filled glovebox ($O_2 < 0.1$ ppm, $H_2O < 0.5$ ppm). Bulk reactions were prepared by grinding together the reagent powders with an agate mortar and pestle, pelletizing the mixture by cold-pressing in a 0.25 inch die at 300 MPa (approximately 100–200 mg per pellet), loading the pellet into a cylindrical alumina crucible held horizontally in an alumina boat, and loading the boat into a mullite or quartz process tube. A Zr foil cap was fit into the mouth of the alumina crucible to decrease Mg_3N_2 loss by volatization and to sacrificially react with any trace O_2. Without air exposure, the samples were reacted in a tube furnace under flowing purified N_2 (*ca.* 20 mL min^{-1} flow rate). A diagram for this system is shown in Fig. S1C (ESI†). Reactions were conducted by heating the sample at +10 °C min^{-1} to the dwell temperature, dwelling for approximately 5–20 h at various temperatures up to 1100 °C, and then cooling by switching off the furnace. Samples were recovered into the Ar glovebox. This procedure was adapted from the strategy used by Verrelli, *et al.*, to synthesize $MgMoN_2$.[22]

Powder X-ray diffraction (PXRD) measurements were performed using a Bruker DaVinci diffractometer with Cu Kα X-ray radiation. All samples were prepared for PXRD from within the glovebox by placing powder on off-axis cut silicon single crystal wafers to reduce the background, and then covered with polyimide tape to slow exposure to the atmosphere. However, as PXRD showed that the product ($MgWN_2$) is air stable, a PXRD pattern was collected without tape to minimize the large scattering background (Fig. 1).

2.2 Thin film synthesis, annealing, and characterization

Combinatorial co-sputtering of Mg–W–N film libraries were conducted in two custom vacuum chambers, both with base pressures of $<10^{-7}$ Torr. Mg and W targets (2 inch diameter, Kurt J. Lesker, 99.95% purity) were angled towards a stationary substrate and sputtered using radiofrequency (RF) excited plasma of the Ar/N_2 gas mixture in the chamber. Sputter powers ranged from 30 W to 90 W for each target, to shift the Mg/(Mg + W) ratio across the whole composition window. Gases were introduced at 50 sccm Ar and 50 sccm N_2, with a 10 Torr process pressure during deposition. The N plasma intensity was enhanced by a RF plasma source at 350 W. Most samples were deposited on 2 inch by 2 inch (001)-oriented Si substrates. Select samples were deposited on insulating substrates (*e.g.*, 100 nm SiO_2 on Si or 100 nm SiN_x on Si) for electronic property measurements, as indicated in the text. Select samples were coated with a 15 nm TiN capping layer, sputtered from a 2 inch diameter Ti target, to protect against atmospheric exposure. During these capping depositions, the substrate was rotated to ensure a homogeneous capping layer. A diagram for this experimental setup is shown in Fig. S1A (ESI†).

Rapid thermal annealing (RTA) experiments were conducted on individual compositionally-graded library rows in flowing N_2 atmosphere at ambient pressure. Heating profiles started with a +100 °C min^{-1} ramp to 100 °C and a 3 min dwell to drive off adsorbed water, followed by a +100 °C min^{-1} ramp to a T_{anneal} set-point in the 600–1200 °C range for a 3 min dwell. Samples were cooled by turning off the heating source. Annealing times

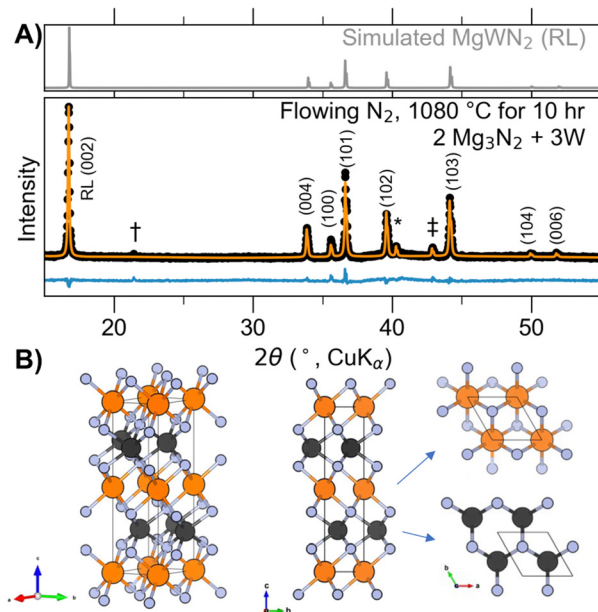**11452** | *J. Mater. Chem. C*, 2023, **11**, 11451–11459

This journal is © The Royal Society of Chemistry 2023

Fig. 1 (A) Rietveld refinement (orange trace) of a PXRD pattern (black dots) of RL $MgWN_2$ produced by heating $2Mg_3N_2 + 3W$ (100% excess Mg_3N_2) under flowing N_2 for 10 h at 1080 °C. The difference trace is shown in blue. The simulated pattern of RL $MgWN_2$ is shown for reference in the box above. W (*), MgO (‡), and an unidentified phase (†) are trace impurities in the pattern. (B) Ball-and-stick models of RL $MgWN_2$ from different perspectives.

were kept short to minimize Mg evaporation at elevated temperatures. A diagram for this experimental setup is shown in Fig. S1B (ESI†).

Combinatorial libraries were measured using the standard 4 × 11 grid employed at NREL, with data analysis conducted using the COMBIgor software package.[23] Each library was mapped with X-ray diffraction (XRD) using a Bruker D8 Discover with Cu Kα radiation and an area detector. Select samples were measured by high-resolution synchrotron grazing incidence wide angle X-ray scattering (GIWAXS) at the Stanford Synchrotron Radiation Lightsource (SSRL) at a wavelength of 0.9744 Å with a Rayonix MX225 CCD area detector, a 3° incident angle, and a 50 μm × 150 μm spot size. GIWAXS detector images were integrated with GSAS-II.[24]

Compositional analysis was performed with X-ray fluorescence (XRF) and Rutherford Back-Scattering (RBS). Metal ratios were mapped using a Bruker M4 Tornado XRF with a Rh source operating at 50 kV and 200 μA. The spot size was 25 μm in diameter. The measurements were performed under vacuum (<20 mbar) with an exposure time of 200 s for each measurement. Nitrogen and oxygen ratios for select samples were quantified with RBS. RBS was run in a 168° backscattering configuration using a model 3S-MR10 RBS system from National Electrostatics Corporation with a 2 MeV He^+ beam energy. Samples were measured for a total integrated charge of 160 μC. RBS spectra were modeled with the RUMP software package.[25]

2.3 Structural analysis of diffraction data

Full-pattern fitting of thin film GIWAXS and bulk PXRD data was performed using TOPAS v6.[26] For thin film samples, 2D diffraction images showed texturing (*i.e.*, preferred orientation),

meaning that integrated peak intensities may not directly correspond to electron density. Therefore, we performed LeBail fits using the appropriate space group and refined lattice parameters, crystallite size broadening (Lorentzian), and strain broadening (Gaussian). For the $MgWN_2$ phase in the RL structure, a model was created by substituting W for Mo in the previously reported $MgMoN_2$ structure in space group $P6_3/mmc$.[22] Rietveld analysis was then performed on bulk PXRD data to refine the lattice parameters, crystallite size broadening, site occupancy, and thermal parameters. In all cases, 10-term polynomial functions were refined to fit the background. Structural visualizations were performed with VESTA.[27]

2.4 Thin film property measurements

Room temperature resistivity was measured on thin films using a custom-built collinear four-point probe instrument by sweeping current between the outer two pins while measuring voltage between the inner pins (1 mm between each pin). Conventional geometric corrections were applied to convert the measured resistance into sheet resistance and then resistivity.[28] The measured films were deposited in a van der Pauw geometry on insulating substrates (either 100 nm thick SiO_2 on Si or 100 nm thick SiN_x on Si) to avoid contribution from the substrates.

Temperature-dependent electrical resistivity was measured on thin films using a Lake Shore Cryotronics Model 8425. For compositions near $MgWN_2$, indium contacts were pressed onto the films. Indium contacts were non-ohmic on Mg_3WN_4 films, so Ti/Au contacts were deposited by evaporation. Temperature-dependent sheet resistance was measured from 104 K to 298 K for most samples, with RL $MgWN_2$ measured from 36 K to 298 K. Resistivity was calculated using XRF-measured film thickness.

2.5 Computational methods

Formation energies were calculated using density functional theory (DFT) using the corrected generalized gradient approximation (GGA + U) implemented in the Vienna *Ab initio* Structural Package (VASP). These calculated values were sourced from the Materials Project when available (v2021.11.10).[29,30] Calculations for additional structures that were not already in the Materials Project database (*i.e.*, all $MgWN_2$ polymorphs, RS and h-BN Mg_3WN_4) were conducted using Atomate (v1.0.3)[31] and Fireworks (v2.0.2)[32] to execute the structure optimization workflow with compatibility with Materials Project entries. DFT calculations require full site occupancy, preventing direct calculation on disordered structures (in which sites have fractional occupancy of different elements). Therefore, calculations were carried out on cation-ordered versions of the experimentally observed cation-disordered structures (*e.g.*, γ-$LiFeO_2$ structure for RS $MgWN_2$). Pymatgen (v2022.4.19) was used to construct the ternary phase diagram shown in Fig. 4.[33]

3 Results and discussion

3.1 Bulk synthesis of cation-ordered $MgWN_2$

Bulk syntheses yielded $MgWN_2$ in a cation-ordered layered hexagonal crystal structure (Fig. 1) previously reported for

This journal is © The Royal Society of Chemistry 2023

J. Mater. Chem. C, 2023, **11**, 11451–11459 | **11453**

$MgMoN_2$.[22,34] We call this structure "rocksaline" (RL) for short, a portmanteau of rocksalt and nickeline, because this structure has interleaved layers of octahedrally-coordinated Mg^{2+} (rocksalt-like) and W^{4+} in a trigonal prismatic site (nickeline-like). The RL $MgWN_2$ phase formed as a black powder from a reaction between Mg_3N_2 and W powders in a 2 : 3 ratio heated at 1080 °C for 10 h. As the balanced reaction is $Mg_3N_2 + 3W + 2N_2 \rightarrow 3MgWN_2$, this synthesis requires a full excess equivalent of Mg_3N_2 to proceed to completion. Still, W often persisted as an impurity owing to the volatility of Mg at elevated temperatures and the refractory nature of W. Syntheses conducted at temperatures <1000 °C did not induce reaction, suggesting a significant kinetic barrier to reactivity between Mg_3N_2 and W. Reactions starting from the elements (*i.e.*, Mg + W under flowing N_2) resulted in uncontrolled Mg loss along with Mg_3N_2 formation, showing that Mg_3N_2 (melting point *ca.* 1500 °C) is a better precursor choice than Mg (melting point 650 °C) for these syntheses.

A Rietveld refinement to probe the degree of site inversion (*x*) for $(Mg_{1-x}W_x)(W_{1-x}Mg_x)N_2$ led to $x = 0.115(10)$, suggesting some cation disorder (Table S1, ESI†). For comparison, $x = 0.5$ would indicate complete cation disorder, and $x = 0$ would indicate a fully ordered phase. However, site occupancy is modeled by fitting relative peak intensities, and peak intensities also vary with preferred orientation which may be present in these data but which was not included in the model.[35] Cation ordering is most clearly defined by a (002) reflection at $2\theta = 17°$ (Fig. S5, ESI†), and the strong reflection observed in Fig. 1 suggests a substantial degree of cation ordering. The isostructural $MgMoN_2$ synthesized by the same method was modeled to be fully ordered by combined analysis of synchrotron PXRD and neutron powder diffraction data.[22]

The formation of RL $MgWN_2$ by high-temperature ceramic synthesis indicates that the RL polymorph defines the thermodynamic ground state. Excess Mg_3N_2 used in bulk syntheses did not lead to any signs of a more Mg-rich phase (*i.e.*, Mg_3WN_4), so we hypothesize that any ordered configurations of those materials (*e.g.*, an ordered wurtzite structure, $Pmn2_1$) may be destabilized at the elevated temperatures (and thus lower nitrogen chemical potential, μ_N) required for ceramic synthesis. The bulk synthesis results differed from the thin-film work presented next, showing the contrast between different precursor options: diffusion-limited bulk-powders compared to atomically-dispersed films.

3.2 Synthesis of Mg–W–N thin films by combinatorial co-sputtering

Combinatorial co-sputtering from Mg and W targets in a N_2/Ar environment resulted in cation-disordered phases with either the RS or the h-BN structure, as determined by laboratory XRD (Fig. 2). The RS structure shows the greatest degree of stability, crystallizing across a wide range of compositions (0.1 < Mg/(Mg + W) < 0.9) and substrate temperatures (up to 600 °C). At elevated substrate temperatures (*ca.* 700 °C), Mg volatilizes, leaving behind metallic W. At Mg/(Mg + W) ratios near 0.75 (*i.e.*, Mg_3WN_4), a h-BN structure is observed in some libraries; it was characterized in greater detail by GIWAXS (Fig. 2B). This h-BN structure only appeared in depositions using one of the custom
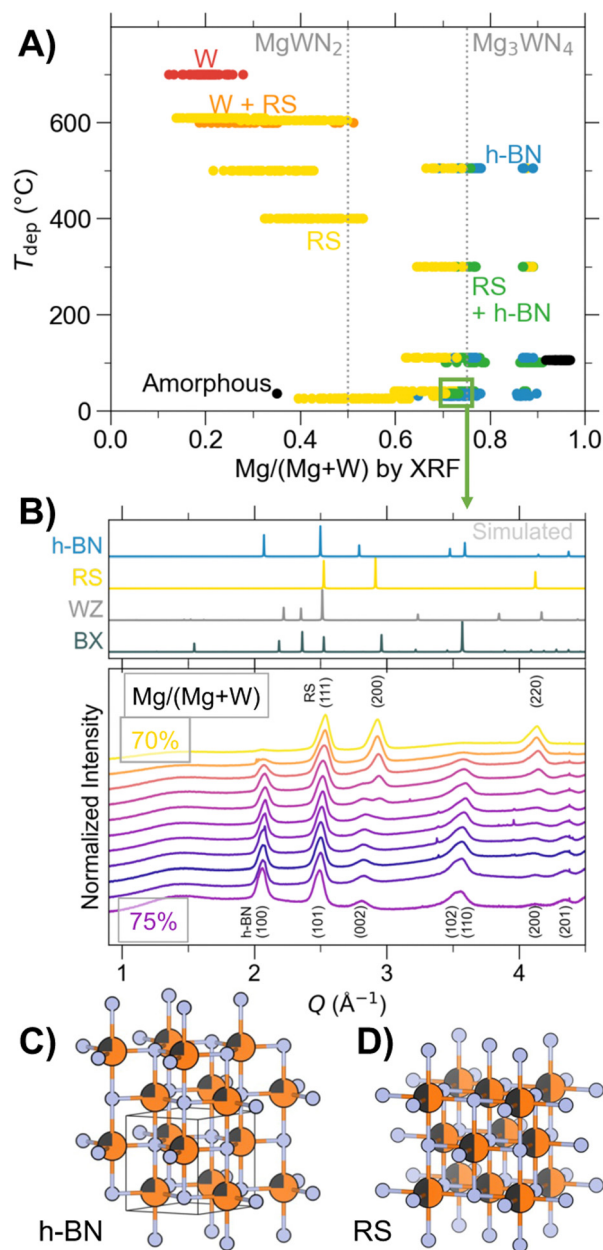

Fig. 2 (A) Phase diagram of thin film Mg–W–N extracted from combinatorial growths at various temperatures (T_{dep}). (B) GIWAXS patterns from a library deposited at ambient conditions, showing the transition between the rocksalt (RS) and h-BN structures. The wurtzite (WZ) and anti-bixbyite (BX) structures are not observed. Ball-and-stick models of (C) h-BN Mg_3WN_4 and (D) RS $MgWN_2$.

vacuum chambers, but not the other. This suggests a subtle (and yet-undetermined) process parameter, such as nitrogen-plasma density or oxygen content, may play a role. RBS and AES measurements on a select few samples show that the measured h-BN Mg_3WN_4 sample contained moderate oxygen content (O/(N + O)) of approximately 15%, Fig. S6, ESI†) while the RS Mg_3WN_4 samples that we measured exhibited much lower oxygen content (Fig. S7, ESI†). However, we cannot definitively conclude that oxygen is essential for stabilization of h-BN Mg_3WN_4 based on a few select measurements. Even within

11454 | *J. Mater. Chem. C*, 2023, **11**, 11451–11459

This journal is © The Royal Society of Chemistry 2023

the one chamber that yielded h-BN Mg_3WN_4, some Mg-rich samples still show the RS structure (Fig. 2), suggesting these two polymorphs may be close in energy. Other Mg-rich points did not exhibit any crystalline phases and are marked as amorphous in Fig. 2A.

The coexistence of h-BN and RS polymorphs near the Mg_3WN_4 stoichiometry suggests the phases may be energetically similar for this Mg/(Mg + W) ratio. Indeed, they are structurally related, with the h-BN structure being an intermediate in a displacive transformation between the RS and WZ structures.[36] This h-BN structure is uncommon among ternary nitrides. The only prior report we can identify in literature is that of Zn-rich compositions for $ZnZrN_2$.[10] However, the five-fold coordination environment of the h-BN is analogous to the transition state experienced by WZ-type ferroelectric materials (*e.g.*, $Al_{1-x}Sc_xN$) as they undergo switching.[37] As another example of a similar motif, $Mg_3Al_3N_5$ has an Al^{3+} ion split across two face-sharing tetrahedral sites,[38] which is structurally similar to the WZ → h-BN → WZ displacement of ferroelectrics. Lastly, a prior study predicted the ground state for Mg_2NbN_3 and Mg_2TaN_3 to be this h-BN structure type,[4] although sputtering experiments subsequently showed that Mg_2NbN_3 crystallizes as a cation-disordered rocksalt.[9,39] The infrequent occurrence of this polymorph suggests decreased stability relative to other high-symmetry phases like the RS polymorph, a hypothesis supported by our RTA experiments (Fig. S3, ESI†) and inability to produce it in bulk.

3.3 Rapid thermal annealing of combinatorial libraries

RTA experiments of combinatorial film libraries show that annealing can induce cation ordering near the $MgWN_2$ stoichiometry (Fig. 3). The samples near the stoichiometric $MgWN_2$ composition retained the RS structure at T_{anneal} = 600 °C, but a clear structure transition to the RL polymorph occurred by T_{anneal} = 900 °C (Fig. 3A). This indicates that the as-deposited RS structure is kinetically stable up to moderately high temperatures (*ca.* 600 °C). High temperatures (*ca.* 900 °C) are needed to allow local diffusion of the randomly-dispersed metals in octahedral environments (the RS structure) to their energetically-preferred coordination environments (octahedral Mg^{2+} and trigonal prismatic W^{4+} in the RL structure).

For Mg-poor compositions (Mg/(Mg + W) < 0.4), annealing produced a slightly different structure than the RS observed in depositions at elevated temperatures, a structure we call WN_x. XRD patterns show two reflections that are similar to the RS (111) and (200) reflections, but which are spaced by slightly too large a gap in 2θ to be consistent with the $Fm\bar{3}m$ structure (Fig. S2, ESI†). However, we are not able to precisely identify the space group of this phase. Only two reflections were detected, and diffraction images show substantial texturing, which suggests that additional reflections may exist outside the measured χ range. Furthermore, the W–N binary system is complex, with 13 unique structures reported in the Inorganic Crystal Structure Database (ICSD) ranging in composition from W_2N to WN_2.[40–44] Given this complexity and ambiguity, we simply refer to these Mg-poor phases as WN_x. This difference may stem from the elevated nitrogen chemical potential present in combinatorial
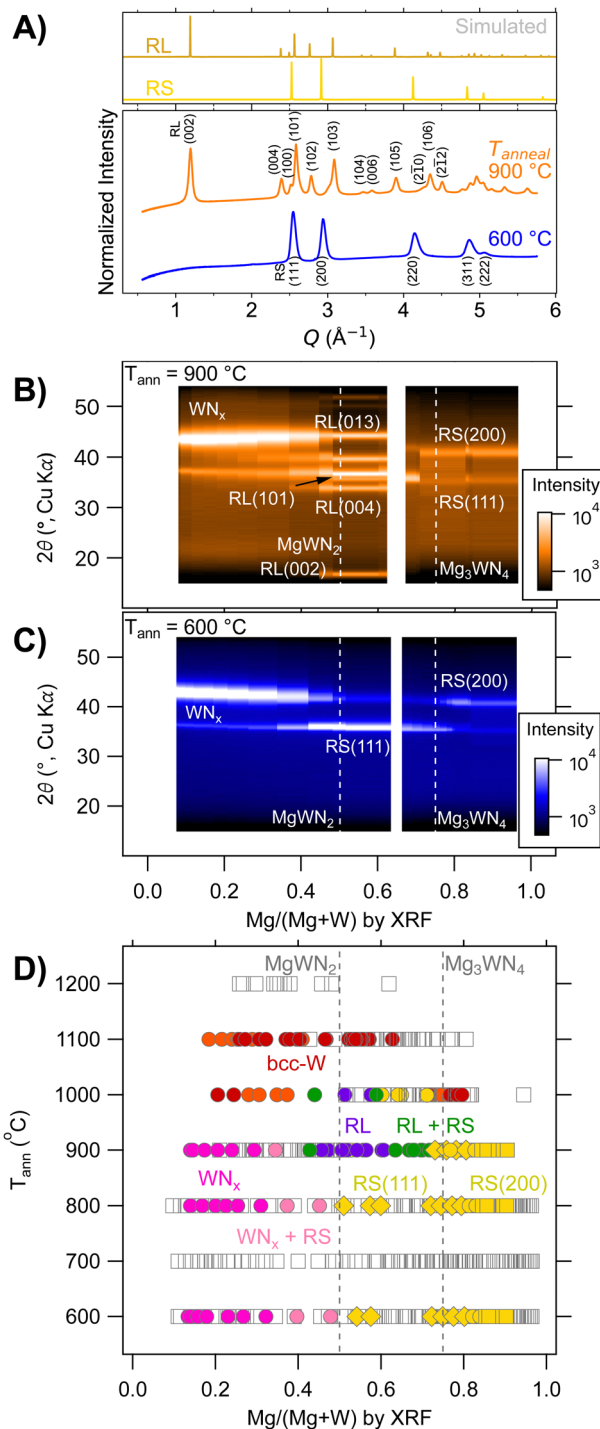

Fig. 3 (A) Synchrotron GIWAXS patterns of $MgWN_2$ annealed at 600 °C and 900 °C. (B) and (C) Laboratory XRD heatmaps as a function of Mg/(Mg + W) for library rows annealed at 600 °C and 900 °C. Labels for the (100) and (102) RL $MgWN_2$ reflections are omitted for clarity. (D) Phase diagram of Mg–W–N depositions as a function of annealing temperature. Samples which were manually identified are indicated by colored markers. Empty markers were not manually labeled but were measured by XRF and XRD, and phases can be inferred from neighboring points.

depositions but absent during annealing, which may affect how much nitrogen is present in the film.[14,45] However, annealed

samples labeled RS in Fig. 3D (*i.e.*, those with Mg/(Mg + W) ≥ 0.5) are well fit with the *Fm*$\bar{3}$*m* space group.

The RS to RL transformation only occurs in a narrow composition window near Mg/(Mg + W) = 0.5 (*i.e.*, MgWN$_2$, Fig. 3D). For Mg-poor compositions with Mg/(Mg + W) < 0.42 and Mg-rich compositions with Mg/(Mg + W) > 0.62, the WN$_x$ and RS structures persisted at T_{anneal} = 900 °C. This shows that the ordered RL structure has a narrow compositional tolerance, while the WN$_x$ and RS structures can accommodate a large degree of off-stoichiometry. These results, along with the thermodynamic calculations presented next (Fig. 4) confirm that the RL phase is the thermodynamic ground state up to approximately 1000 °C, as initially shown by bulk syntheses.

3.4 Thermodynamic analysis

Calculated formation energies relative to the binaries show that RL MgWN$_2$ is the only thermodynamically stable ternary in the Mg–W–N system, according to DFT calculations of the cation-ordered structures (Fig. 4). The striking favorability of the RL polymorph of MgWN$_2$ is driven by the electronic preference of d^2 metals (like W^{4+}) for trigonal prismatic coordination environments.[47] In brief, the ligand field splitting of the trigonal prismatic coordination environment lowers the energy of the highest occupied d orbitals (compared to the octahedral environment). The electronic origin of this RL favorability should have consequences for electronic properties, as discussed in section 3.5. The next lowest energy polymorph for MgWN$_2$ is RS, followed by h-BN, then WZ. This trend suggests

that lower coordination numbers lead to higher polymorph energies, as the cations in the RS, h-BN, and WZ structures are coordinated by 6, 5, and 4 anions, respectively. In the case of the Mg$_3$WN$_4$ stoichiometry, all three polymorphs (RS, h-BN, and WZ) are much closer to the hull than the metastable MgWN$_2$ polymorphs, yet they are still slightly metastable. A RS Mg$_3$WN$_4$ structure (space group *I4/mmm*) is closest to the hull (+0.031 eV per atom above the hull), but the h-BN structure is only slightly higher in energy (+0.034 eV per atom above the hull). The WZ-derived phase of Mg$_3$WN$_4$, with a desirable predicted bandgap of *ca.* 5 eV,[1] is only slightly higher (+0.063 eV per atom above the hull). Just as with MgWN$_2$, the trend for Mg$_3$WN$_4$ is consistent with lower coordination numbers leading to higher polymorph energies. However, for the Mg$_3$WN$_4$ stoichiometry, the trigonal prisms of RL MgWN$_2$ no longer provide an energetic benefit.

The DFT calculations shown in Fig. 4 agree with our synthetic results. RL MgWN$_2$ was the only ternary phase formed by bulk synthesis, where high temperatures are sufficient to overcome kinetic barriers to produce thermodynamic ground-state phases. The formation of RS MgWN$_2$ by combinatorial sputtering is also consistent with the trend from calculations and with prior literature.[9,10] In the case of physical vapor deposition methods (like sputtering), atoms arrive at the film surface in a disordered configuration (*i.e.*, high effective temperature). Under these conditions, configurational entropy favors structures with a single type of cation site (like RS, h-BN, and WZ) and enthalpy penalizes structures with two or more distinct cation sites (like RL), as demonstrated for the Zn–Zr–N system.[10] In other words, RS is a disorder-tolerant structure that becomes energetically favorable under sputtering synthesis conditions. While we do not consider disorder in the calculations shown in Fig. 4B, the ordered RS phase is lower in energy than the ordered WZ or h-BN phases, suggesting Mg^{2+} and W^{4+} prefer octahedral coordination environments over tetrahedral (WZ) and trigonal bipyramidal (h-BN) environments. Lastly, oxygen substitution on nitrogen sites is common in nitrides,[1,18] and these materials are no exception. RBS measurements detect O/(N + O) = 15% for Mg$_3$WN$_4$ with a h-BN structure (Fig. S6, ESI†). Auger electron spectroscopy measurements on Mg$_3$WN$_4$ with a RS structure detect lower levels of oxygen (O/(N + O) < 2%, Fig. S7, ESI†). These measurements suggest that oxygen incorporation may stabilize the h-BN structure over the RS structure for Mg$_3$WN$_4$. Oxygen impurities affect the energy landscape but are not accounted for in these calculations.

3.5 Electronic properties

The polymorphic differences for MgWN$_2$ should lead to different properties. To assess this possibility, we conducted electronic structure calculations on the cation-ordered RL polymorph and a cation-ordered model of RS MgWN$_2$. As these electronic structure calculations cannot be conducted on disordered models, we created a cation-ordered RS MgWN$_2$ phase based on the γ-LiFeO$_2$ structure type (space group *I4$_1$/amd*). Other ordered structures could also be used (*i.e.*, α-NaFeO$_2$, β-LiFeO$_2$, or Li$_2$Ti$_2$O$_4$),[48] but the octahedral coordination of W^{4+} would
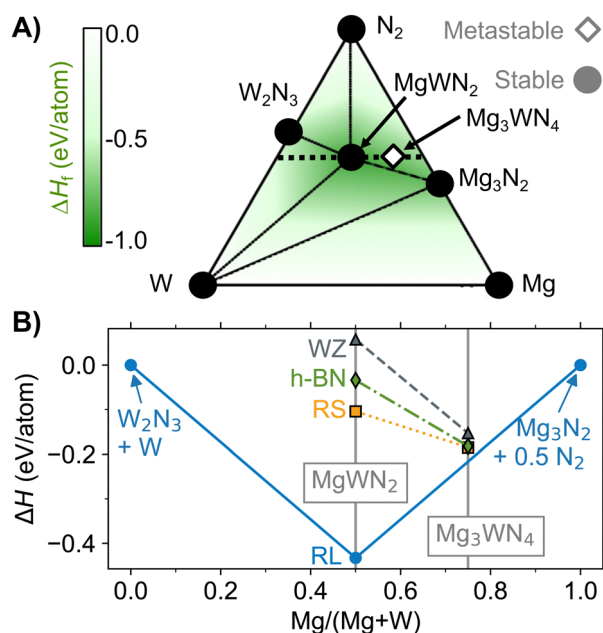

Fig. 4 (A) Ternary phase diagram for the Mg–W–N system calculated using pymatgen.[33] (B) Pseudobinary isopleth calculated with a cation : anion ratio of 1 : 1 (corresponding to the black dotted trace from (A). The vertical axis shows the relative formation energy (Δ*H*) at *T* = 0 k compared to the most stable point in the binary hulls at this cation:anion ratio (W$_2$N$_3$ + W and Mg$_3$N$_2$ + 1/2N$_2$). Several highly metastable ternary phases in the NREL MatDB and materials project databases are omitted for clarity.[30,46]

11456 | *J. Mater. Chem. C*, 2023, **11**, 11451–11459

This journal is © The Royal Society of Chemistry 2023

still define the states at the Fermi level in each version. Calculated density of states (DoS) diagrams show that RS $MgWN_2$ has states at the Fermi level and should exhibit metallic behavior, while RL $MgWN_2$ is calculated to be a semiconductor with a 1.18 eV bandgap (Fig. 5). As we used the GGA + U functional for this DFT (not a hybrid functional), this 1.18 eV bandgap is likely an underestimate. This latter finding is consistent with the 0.7 eV bandgap calculated for RL $MgMoN_2$ (also calculated without the use of hybrid functionals),[22] and with the band structure of MoS_2, where Mo^{4+} takes a trigonal prismatic coordination environment.[49,50] Band structure diagrams are shown in Fig. S9 and S10 (ESI†).

This difference can be rationalized *via* a simple ligand field splitting model. The RL polymorph has the $5d^2$ valence electrons fully occupying a d_{z^2} orbital (Fig. 5B). The lowest unoccupied orbitals are degenerate $d_{x^2-y^2}$ and d_{xy}, suggesting a bandgap defined by d–d transitions. This splitting provides an electronic explanation for the thermodynamic favorability of the RL structure for d^2 transition metals.[47] In contrast, the W^{4+} in the RS polymorph undergoes octahedral ligand field splitting. That leads to metallic conductivity *via* three degenerate orbitals (d_{xy}, d_{xz}, and d_{yz}) for the $5d^2$ valence electrons (Fig. 5D). Such splitting is consistent with the calculated DoS, where W states make up a large fraction of the valence and conduction bands for RL $MgWN_2$ and states near the Fermi level for RS $MgWN_2$.

Temperature-dependent resistivity measurements of thin films indicate semiconducting behavior for RL $MgWN_2$ and RS Mg_3WN_4 (Fig. 6A). Resistivity decreases with increasing temperature for both samples, although the trend for $MgWN_2$ is significantly weaker than for Mg_3WN_4 (Fig. S10, ESI†). This trend suggests thermally activated charge transport. The semiconductivity of RS Mg_3WN_4 is consistent with the 6+ oxidation state for W in that phase ($5d^0$ electron configuration). The change in slope near 230 K is an artefact of the instrument that we have observed for numerous films and substrates in this instrument.[51–54] The resistivity of RL $MgWN_2$ is low (*ca.* 0.001 Ω cm), suggesting a high level of doping and/or a small

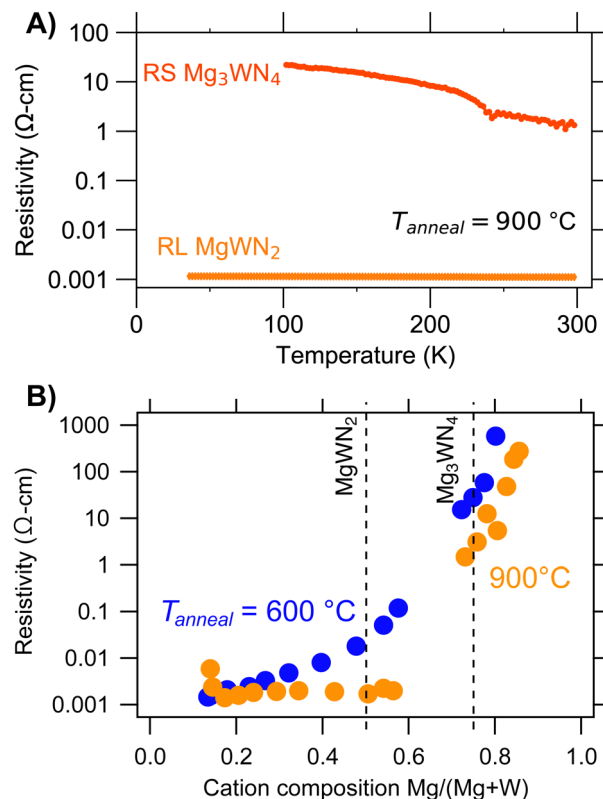Fig. 5 Calculated density of states (dos) for the (A) RL $MgWN_2$ and (C) rs $MgWN_2$ (calculated using the ordered structure with space group $I4_1/amd$. Ligand field splitting diagrams for W^{4+} in (B) trigonal prismatic and (D) Octahedral environments.

Fig. 6 (A) Temperature-dependent resistivity measurements of select samples of RS Mg_3WN_4 and RL $MgWN_2$ (T_{anneal} = 900 °C). (B) Colinear four-point probe measurements of Mg–W–N library rows annealed at 600 °C and 900 °C.

bandgap. The resistivity of RS Mg_3WN_4 is substantially larger, indicating a lower dopant content and/or a large bandgap. We were not able to reliably measure temperature-dependent resistivity of RS $MgWN_2$, possibly owing to compositional gradients within the film or sample degradation from air exposure over time. Similar trends in conductivity were observed in the Zn–Mo–N system, where films of a wurtzite structure spanned low-resistivity $ZnMoN_2$ to insulating Zn_3MoN_4.[17] Optical measurements of these metallic-to-semiconductor changes would be interesting for further study, but the opaque silicon substrates and van der Pauw mask geometry used in this study inhibited optical measurements.

Electronic properties of these films are affected by film quality and composition. Room temperature resistivity measurements show that annealing at 900 °C decreases resistivity slightly across the whole composition range (compared to samples annealed at 600 °C), consistent with decreased grain-boundary resistance (Fig. 6B). Additionally, oxygen is present in these films (Fig. S6 and S8, ESI†), which decreases resistivity by introducing charge carriers or increases resisitivity by producing interfacial oxide layers (*i.e.*, MgO). Fig. 6 also shows that resistivity can change dramatically with composition. Resistivity (ρ) increases as a function of Mg content, with Mg-poor samples exhibiting $\rho < 0.01$ Ω cm and Mg-rich samples exhibiting $\rho > 100$ Ω cm. In sum, these trends shows that the Mg–W–N system
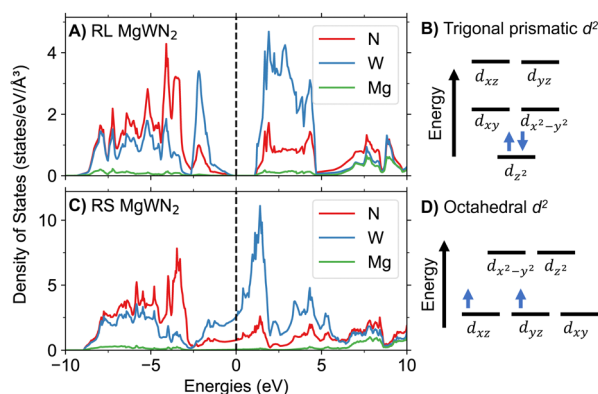
This journal is © The Royal Society of Chemistry 2023

J. Mater. Chem. C, 2023, 11, 11451–11459 | 11457

holds potential for tunable electronic properties, although future work should focus on higher quality films to bring that promise to fruition.

4 Conclusions

We synthesized three new polymorphs of magnesium tungsten nitrides by bulk and film synthesis methods in a previously empty ternary phase space, and demonstrated how rapid thermal annealing can be a powerful tool to reconcile thermodynamic and non-equilibrium synthesis pathways. Combinatorial co-sputtering yielded cation-disordered rocksalt structures across a wide composition range including $MgWN_2$, while samples near the Mg_3WN_4 stoichiometry crystallized in either a cation-disordered rocksalt or a cation-disordered hexagonal boron nitride structure. Rapid thermal annealing treatments of these combinatorial libraries show that rocksalt $MgWN_2$ converted to a cation-ordered rocksaline structure at $T_{anneal} = 900\ ^\circ C$, in a narrow composition window around the nominal stoichiometry. This cation-ordered $MgWN_2$ phase also appeared in bulk ceramic syntheses and was predicted as the ground state structure by theoretical calculations, indicating that annealing of thin film libraries can potentially access the thermodynamically stable ternary nitrides. Density of state calculations suggest cation-disordered rocksalt $MgWN_2$ should exhibit metallic properties while cation-ordered rocksaline $MgWN_2$ should exhibit semiconducting behavior. Resistivity measurements show that rocksaline $MgWN_2$ and rocksalt Mg_3WN_4 are semiconductors, but we were unable to experimentally confirm the metallic behavior of rocksalt $MgWN_2$. Resistivity varies by six orders of magnitude as a function of Mg content. In sum, these findings expand the toolkit through which combinatorial co-sputtering experiments can explore the thermodynamic landscape in search of new nitride compounds.

Author contributions

C. L. R.: conceptualization, investigation, formal analysis, writing – original draft, writing – review & editing, visualization. R. W. S.: investigation, writing – review & editing. C. A. K.: investigation. K. N. H.: investigation, formal analysis, writing – review & editing. J. R. N.: investigation, formal analysis, software, resources, writing – review & editing, supervision, funding acquisition. S. R. B.: methodology, resources, writing – review & editing, supervision. A. Z.: conceptualization, methodology, investigation, resources, writing – review & editing, visualization, supervision, funding acquisition.

Conflicts of interest

There are no conflicts to declare.

Acknowledgements

Notes and references

1 A. L. Greenaway, C. L. Melamed, M. B. Tellekamp, R. Woods-Robinson, E. S. Toberer, J. R. Neilson and A. C. Tamboli, *Annu. Rev. Mater. Res.*, 2021, **51**, 591–618.

2 A. Zakutayev, *J. Mater. Chem. A*, 2016, **4**, 6742–6754.

3 W. Sun, C. J. Bartel, E. Arca, S. R. Bauers, B. Matthews, B. Orvañanos, B.-R. Chen, M. F. Toney, L. T. Schelhas, W. Tumas, J. Tate, A. Zakutayev, S. Lany, A. M. Holder and G. Ceder, *Nat. Mater.*, 2019, **18**, 732–739.

4 A. Zakutayev, S. R. Bauers and S. Lany, *Chem. Mater.*, 2022, **34**, 1418–1438.

5 S. Zhuk, A. A. Kistanov, S. C. Boehme, N. Ott, F. La Mattina, M. Stiefel, M. V. Kovalenko and S. Siol, *Chem. Mater.*, 2021, **33**, 9306–9316.

6 K. N. Heinselman, S. Lany, J. D. Perkins, K. R. Talley and A. Zakutayev, *Chem. Mater.*, 2019, **31**, 8717–8724.

7 A. L. Greenaway, A. L. Loutris, K. N. Heinselman, C. L. Melamed, R. R. Schnepf, M. B. Tellekamp, R. Woods-Robinson, R. Sherbondy, D. Bardgett and S. Bauers, *et al.*, *J. Am. Chem. Soc.*, 2020, **142**, 8421–8430.

8 A. L. Greenaway, S. Ke, T. Culman, K. R. Talley, J. S. Mangum, K. N. Heinselman, R. S. Kingsbury, R. W. Smaha, M. K. Gish and E. M. Miller, *et al.*, *J. Am. Chem. Soc.*, 2022, **144**, 13673–13687.

9 S. R. Bauers, A. Holder, W. Sun, C. L. Melamed, R. Woods-Robinson, J. Mangum, J. Perkins, W. Tumas, B. Gorman and A. Tamboli, *et al.*, *Proc. Natl. Acad. Sci. U. S. A.*, 2019, **116**, 14829–14834.

10 R. Woods-Robinson, V. Stevanovic, S. Lany, K. N. Heinselman, M. K. Horton, K. A. Persson and A. Zakutayev, *Phys. Rev. Mater.*, 2022, **6**, 043804.

11 R. W. Smaha, K. Yazawa, A. G. Norman, J. S. Mangum, H. Guthrey, G. L. Brennecka, A. Zakutayev, S. R. Bauers,

11458 | *J. Mater. Chem. C*, 2023, **11**, 11451–11459

This journal is © The Royal Society of Chemistry 2023

P. Gorai and N. M. Haegel, *Chem. Mater.*, 2022, **34**, 10639–10650.

12 K. R. Talley, C. L. Perkins, D. R. Diercks, G. L. Brennecka and A. Zakutayev, *Science*, 2021, **374**, 1488–1491.

13 W. Yu, H. Li, J. Li, Z. Liu, J. Huang, J. Kong, Q. Wu, Y. Shi, G. Zhang and D. Xiong, *Vacuum*, 2023, **207**, 111673.

14 A. Zakutayev, *J. Phys.: Condens. Matter*, 2021, **33**, 354003.

15 R. Kikuchi, T. Nakamura, T. Kurabuchi, Y. Kaneko, Y. Kumagai and F. Oba, *Chem. Mater.*, 2021, **33**, 8205–8211.

16 A. D. Martinez, A. N. Fioretti, E. S. Toberer and A. C. Tamboli, *J. Mater. Chem. A*, 2017, **5**, 11418–11435.

17 E. Arca, S. Lany, J. D. Perkins, C. Bartel, J. Mangum, W. Sun, A. Holder, G. Ceder, B. Gorman and G. Teeter, *et al.*, *J. Am. Chem. Soc.*, 2018, **140**, 4293–4301.

18 R. R. Schnepf, J. J. Cordell, M. B. Tellekamp, C. L. Melamed, A. L. Greenaway, A. Mis, G. L. Brennecka, S. Christensen, G. J. Tucker and E. S. Toberer, *et al.*, *ACS Energy Lett.*, 2020, **5**, 2027–2041.

19 S. Lany, A. N. Fioretti, P. P. Zawadzki, L. T. Schelhas, E. S. Toberer, A. Zakutayev and A. C. Tamboli, *Phys. Rev. Mater.*, 2017, **1**, 035401.

20 E. W. Blanton, K. He, J. Shan and K. Kash, *J. Cryst. Grow.*, 2017, **461**, 38–45.

21 C. Fetzer, R. Lee, G. Stringfellow, X. Liu, A. Sasaki and N. Ohno, *J. Appl. Phys.*, 2002, **91**, 199–203.

22 R. Verrelli, M. E. Arroyo-de Dompablo, D. Tchitchekova, A. Black, C. Frontera, A. Fuertes and M. R. Palacin, *Phys. Chem. Chem. Phys.*, 2017, **19**, 26435–26441.

23 K. R. Talley, S. R. Bauers, C. L. Melamed, M. C. Papac, K. N. Heinselman, I. Khan, D. M. Roberts, V. Jacobson, A. Mis and G. L. Brennecka, *et al.*, *ACS Comb. Sci.*, 2019, **21**, 537–547.

24 B. H. Toby and R. B. Von Dreele, *J. Appl. Crystallogr.*, 2013, **46**, 544–549.

25 N. Barradas, K. Arstila, G. Battistig, M. Bianconi, N. Dytlewski, C. Jeynes, E. Kótai, G. Lulli, M. Mayer and E. Rauhala, *et al.*, *Nucl. Instrum. Methods Phys. Res., Sect. B*, 2008, **266**, 1338–1342.

26 A. A. Coelho, *J. Appl. Crystallogr.*, 2018, **51**, 210–218.

27 K. Momma and F. Izumi, *J. Appl. Crystallogr.*, 2011, **44**, 1272–1276.

28 F. Smits, *Bell Syst. Tech. J.*, 1958, **37**, 711–718.

29 A. Jain, G. Hautier, S. P. Ong, C. J. Moore, C. C. Fischer, K. A. Persson and G. Ceder, *Phys. Rev. B: Condens. Matter Mater. Phys.*, 2011, **84**, 045115.

30 A. Jain, S. P. Ong, G. Hautier, W. Chen, W. D. Richards, S. Dacek, S. Cholia, D. Gunter, D. Skinner and G. Ceder, *et al.*, *APL Mater.*, 2013, **1**, 011002.

31 K. Mathew, J. H. Montoya, A. Faghaninia, S. Dwarakanath, M. Aykol, H. Tang, I.-H. Chu, T. Smidt, B. Bocklund and M. Horton, *et al.*, *Comput. Mater. Sci.*, 2017, **139**, 140–152.

32 A. Jain, S. P. Ong, W. Chen, B. Medasani, X. Qu, M. Kocher, M. Brafman, G. Petretto, G.-M. Rignanese and G. Hautier, *Concurr. Comput. Pract. Exp.*, 2015, **27**, 5037–5059.

33 S. P. Ong, W. D. Richards, A. Jain, G. Hautier, M. Kocher, S. Cholia, D. Gunter, V. L. Chevrier, K. A. Persson and G. Ceder, *Comput. Mater. Sci.*, 2013, **68**, 314–319.

34 L. Wang, K. Tang, Y. Zhu, Q. Li, B. Zhu, L. Wang, L. Si and Y. Qian, *J. Mater. Chem.*, 2012, **22**, 14559–14564.

35 R. E. Dinnebier, A. Leineweber and J. S. Evans, in *Rietveld Refinement*, de Gruyter, 2018.

36 S. Limpijumnong and W. R. Lambrecht, *Phys. Rev. B: Condens. Matter Mater. Phys.*, 2001, **63**, 104103.

37 S. Fichtner, N. Wolff, F. Lofink, L. Kienle and B. Wagner, *J. Appl. Phys.*, 2019, **125**, 114103.

38 R. Schmidt, M. Ströbele, K. Eichele and H.-J. Meyer, *Eur. J. Inorg. Chem.*, 2017, 2727–2735.

39 P. K. Todd, M. J. Fallon, J. R. Neilson and A. Zakutayev, *ACS Mater. Lett.*, 2021, **3**, 1677–1683.

40 X. Feng, K. Bao, Q. Tao, L. Li, Z. Shao, H. Yu, C. Xu, S. Ma, M. Lian and X. Zhao, *et al.*, *Inorg. Chem.*, 2019, **58**, 15573–15579.

41 C. Wang, Q. Tao, S. Dong, X. Wang and P. Zhu, *Inorg. Chem.*, 2017, **56**, 3970–3975.

42 T. Sasaki, T. Ikoma, K. Sago, Z. Liu, K. Niwa, T. Ohsuna and M. Hasegawa, *Inorg. Chem.*, 2019, **58**, 16379–16386.

43 S. Wang, X. Yu, Z. Lin, R. Zhang, D. He, J. Qin, J. Zhu, J. Han, L. Wang and H.-K. Mao, *et al.*, *Chem. Mater.*, 2012, **24**, 3023–3028.

44 C.-C. Chang, T. Sasaki, N. A. Gaida, K. Niwa and M. Hasegawa, *Inorg. Chem.*, 2021, **60**, 13278–13283.

45 C. M. Caskey, R. M. Richards, D. S. Ginley and A. Zakutayev, *Mater. Horiz.*, 2014, **1**, 424–430.

46 V. Stevanovic, S. Lany, X. Zhang and A. Zunger, *Phys. Rev. B: Condens. Matter Mater. Phys.*, 2012, **85**, 115104.

47 M. Kertesz and R. Hoffmann, *J. Am. Chem. Soc.*, 1984, **106**, 3453–3460.

48 G. C. Mather, C. Dussarrat, J. Etourneau and A. R. West, *J. Mater. Chem.*, 2000, **10**, 2219–2230.

49 R. Kasowski, *Phys. Rev. Lett.*, 1973, **30**, 1175.

50 L. Mattheiss, *Phys. Rev. Lett.*, 1973, **30**, 784.

51 R. W. Smaha, J. S. Mangum, I. A. Leahy, J. Calder, M. P. Hautzinger, C. P. Muzzillo, C. L. Perkins, K. R. Talley, S. Eley and P. Gorai *et al.*, *arXiv*, 2023, *preprint*, arXiv:2305.00098, 2023.

52 S. R. Bauers, D. M. Hamann, A. Patterson, J. D. Perkins, K. R. Talley and A. Zakutayev, *Jpn. J. Appl. Phys.*, 2019, **58**, SC1015.

53 S. R. Bauers, J. Mangum, S. P. Harvey, J. D. Perkins, B. Gorman and A. Zakutayev, *Appl. Phys. Lett.*, 2020, **116**, 102102.

54 C. L. Rom, R. W. Smaha, C. L. Melamed, R. R. Schnepf, K. N. Heinselman, J. S. Mangum, S.-J. Lee, S. Lany, L. T. Schelhas and A. L. Greenaway, *et al.*, *Chem. Mater.*, 2023, **35**, 2936–2946.

This journal is © The Royal Society of Chemistry 2023

J. Mater. Chem. C, 2023, **11**, 11451–11459 | **11459**